Article

Reutilizing Methane Reforming Spent Catalysts as Efficient Overall Water-Splitting Electrocatalysts

Muhammad Awais Khan, Muhammad Taqi Mehran,* Salman Raza Naqvi, Asif Hussain Khoja,
Faisal Shahzad, Umair Sikander, Sajjad Hussain, Ramsha Khan, Bilal Sarfaraz,
and Mutawara Mahmood Baig

Read Online

| ACCESS | | Metrics & More | | Article Recommendations | | Supporting Information |

ABSTRACT: It is extremely prudent and highly challenging to design a greener bifunctional electrocatalyst that shows effective electrocatalytic activity and high stability toward electrochemical water splitting. As several hundred tons of catalysts are annually deactivated by deposition of carbon, herein, we came up with a strategy to reutilize spent methane reforming catalysts that were deactivated by the formation of graphitic carbon (GC) and carbon nanofibers (CNF). An electrocatalyst was successfully synthesized by in situ deposition of noble metal-free MoS_2 over spent catalysts via a hydrothermal method that showed exceptional performance regarding the hydrogen evolution reaction (HER) and the oxygen evolution reaction (OER). At 25 mA cm^{-2}, phenomenal OER overpotentials (η_{25}) of 128 and 154 mV and modest HER overpotentials of 186 and 207 mV were achieved for MoS_2@CNF and MoS_2@GC, respectively. Moreover, OER Tafel slopes of 41 and 71 mV dec^{-1} and HER Tafel slopes of 99 and 107 mV dec^{-1} were obtained for MoS_2@CNF and MoS_2@GC, respectively. Furthermore, the synthesized catalysts exhibited good long-term durability for about 18 h at 100 μA cm^{-2} with unnoticeable changes in the linear sweep voltammetry (LSV) curve of the HER after 1000 cycles. The carbon on the spent catalyst increased the conductivity, while MoS_2 enhanced the electrocatalytic activity; hence, the synergistic effect of both materials resulted in enhanced electrocatalysts for overall water splitting. This work of synthesizing enhanced nanostructured electrocatalysts with minimal usage of inexpensive MoS_2 gives a rationale for engineering potent greener electrocatalysts.
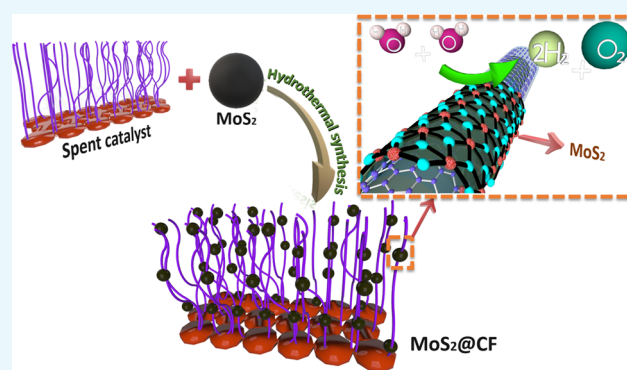
INTRODUCTION

We have entered a new era in which planetary changes are primarily driven by humans instead of natural forces, resulting in a predatory relationship where the natural environment has become prey to drastic anthropic activities that lead up to greenhouse gas emissions and global warming.[1] This human–environment relationship can be harmonized by shifting our energy reliance from fossil fuels to greener, sustainable, and renewable energy vectors like hydrogen.[2,3] Hydrogen is pacing up to lead the global race of energy requirement, with an increasing current demand of 70 Mt of H_2/year.[4−6] Currently, emission-intensive processes predominantly used for hydrogen production are methane reforming (i.e., produces 7 kg CO_2/kg H_2) and coal gasification (i.e., produces 18−20 kg CO_2/kg H_2), which results in wasting a large amount of catalyst due to the growth of carbon over the catalyst surface.[7−11] In 2009, it was reported that about 150 000−170 000 tons of catalyst from hydroprocessing was deactivated or spent annually, with about an annual increase of 5%, which is predicted to be now in the range of 232 500−263 500 t/year.[12−15] Depending on the process parameters, carbon can grow on the surface of spent

catalysts with different morphologies such as graphitic sheets, nanorods, nanotubes, or nanofibers.[16−19] The diverse morphologies of carbon on spent catalysts increase the available surface area of the spent catalysts, which can provide a better spot for the deposition of any efficient electrochemical water-splitting catalyst (Figure 1).[20−22]

Typically, noble metal-based catalysts such as IrO_2, RuO_2, and Pt are considered the most efficient catalysts for the oxygen evolution reaction (OER) and the hydrogen evolution reaction (HER).[23−26] However, the terrestrial scarcity and high material cost of these noble catalysts have limited their use as electrocatalysts.[27,28] Recently, robust, earth-abundant, and cheap transition metal dichalcogenides (TMDs) with a general formula of MX_2 (M = transition metal, X = chalcogen) have been
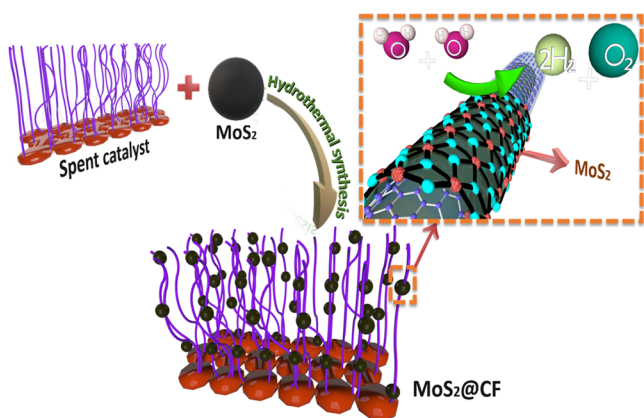
Figure 1. Schematic illustration for utilizing the spent reforming catalyst for electrochemical water splitting.

uncovered, showing promising electrocatalytic activity.[29−32] Amid these TMDs, MoS_2 has grabbed attention due to its high theoretical catalytic activity, low cost, and greater electrochemical stability. However, it is well known that the two major constraints that limit the further enhancement of MoS_2 activity are the low electrical conductivity and highly inert basal plane of MoS_2.[33−35][33−35] These shortcomings have been curbed through immense research in which 2H-MoS_2 (i.e., a semiconductor with a band gap of about 1.9 eV) is replaced with nanostructured 1T-MoS_2 with 10^7 times more conductive because the 4D orbital in 1T-MoS_2 is incompletely filled.[36,37] Supporting MoS_2 with highly conductive nanomaterials like graphene sheets, carbon nanotubes, nanocages, and nanofibers further aids in the enhancement of the HER and OER performance.[38−42]
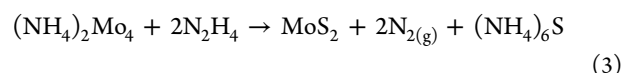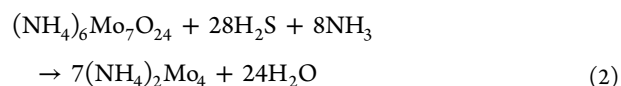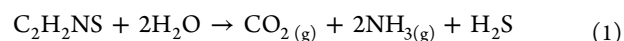
In this research, spent methane reforming catalysts were reutilized for developing electrocatalysts. The methane reforming catalyst was obtained from a previous study, i.e.,[43] where it got spent due to the growth of carbon over the surface of the reforming catalyst. The carbon on the spent catalyst was having two different morphologies: one sample of the spent catalyst possessed graphitic carbon (GC), while the other sample consisted of carbon nanofibers (CNF). Noble metal-free MoS_2 was deposited on the surface of these obtained spent catalysts, via an in situ hydrothermal method. The obtained electrocatalyst majorly comprised the spent catalyst with MoS_2 deposited over its surface.

EXPERIMENTAL SECTION

Reagents. Ammonium heptamolybdate ((NH_4)$_6Mo_7O_{24}$.4H_2O, CAS number: 12054-82-2, purity = 99.0%) was purchased from Daejung. Thioacetamide (C_2H_2NS, reagent grade, CAS number: 62-55-5) was purchased from SCHARLU. Ni foam (>99.0%) was purchased from Sigma-Aldrich, acetone (>99.8%) from VWR Chemicals, and ethanol (>99.9%) from Labscan Asia Co. Ltd.

Preparation of the Electrocatalyst. The final electrocatalyst of MoS_2 on the spent catalyst was synthesized by adopting the in situ hydrothermal method. This synthesis method involved the in-process growth of MoS_2 on the spent catalyst. (NH_4)$_6Mo_7O_{24}$.4H_2O (0.14 mmol) and 2.3 mmol of C_2H_2NS were dissolved in about 50 mL of deionized (DI) water. Three milliliters of hydrazine hydrate was added to the solution dropwise. For maintaining the pH of the solution, hydrogen chloride (HCl) was added to the solution. About 10 g of the spent catalyst was added to the mixture. After vigorous stirring

for about 2 h at 800 rpm, the mixture was transferred to a Teflon-lined autoclave, which was then heated at 200 °C for about 24 h. The autoclave was allowed to cool naturally under room temperature. The resulting black mixture was sonicated, centrifuged, and washed with ethanol and DI water after which it was dried overnight at 80 °C. In this process, MoS_2 was obtained from the reaction of (NH_4)$_6Mo_7O_{24}$.4H_2O and C_2H_2NS with water. Ammonium heptamolybdate tetrahydrate served as a source of molybdenum, while thioacetamide provided the sulfur required. Following reactions occurred forming intercalated MoS_2.[44]

$$C_2H_2NS + 2H_2O \rightarrow CO_{2\,(g)} + 2NH_{3(g)} + H_2S \tag{1}$$

$$(NH_4)_6Mo_7O_{24} + 28H_2S + 8NH_3$$
$$\rightarrow 7(NH_4)_2Mo_4 + 24H_2O \tag{2}$$

$$(NH_4)_2Mo_4 + 2N_2H_4 \rightarrow MoS_2 + 2N_{2(g)} + (NH_4)_6S \tag{3}$$

Preparation of Ink and Synthesis of the Electrode. The ink for electrochemical testing was prepared by taking the sample of the decorated spent catalyst, carbon black, and poly(vinylidene fluoride) (PVDF) in a ratio of 85:10:5. First, PVDF was sonicated in NMP for about 2 h. Then, carbon black and the prepared sample were added and again sonicated for about 4 h, which resulted in black ink. About 50 μL of the prepared ink was taken with the help of a micropipette and then deposited on the treated nickel foam with an area of 1 cm^2. The nickel foam was used as a substrate, which was treated by sonicating it in acetone, 2 M HCl, and absolute ethanol, consecutively, for 15 min in each solution. The Ni foam was dried at 60 °C in a drying oven for 2 h. The ink-loaded foam was dried at 80 °C for about 12 h. The loading on the nickel foam was noted by weighing it before and after deposition of the ink, which varied from 2.1 to 2.8 mg for all samples and this variation was due to the change in the density of samples before and after deposition.

Characterization of Materials. An STOE-Seifert X'Pert PRO was used for X-ray diffraction (XRD) characterization with 2θ values ranging from 5 to 80° using Cu Kα radiation. Morphological characterization was performed by scanning electron microscopy (SEM) and energy-dispersive X-ray spectroscopy (EDX) mapping for which a JEOL instrument JSM-6490A was used. Analytical information was studied by Fourier transform infrared (FT-IR) spectroscopy for which an iS50 FT-IR spectrometer, Thermo Scientific was used.

Electrochemical Measurements. Electrochemical testing of the sample was performed using a Biologic potentiostat with a three-electrode cell. Platinum (Pt) gauze was used as a counter electrode, while Ag/AgCl was used as a reference electrode. The electrochemical cell setup showing the reference, working, and counter electrodes is shown in Figure S1 (Supporting Information) The prepared loaded Ni foam was used as the working electrode. Potassium hydroxide (KOH, 1 M) was used as the electrolyte. Cyclic voltammetry (CV) was performed at 10, 20, 40, and 50 mV s^{-1} in a voltage range of −0.4−0.6 V. For ease and further calculations, reversible hydrogen electrode (RHE) potential was used which was obtained using $E_{RHE} = E_{Ag/AgCl} + 0.059\,pH + 0.1976$, with pH = 14. For computing resistance, the electrochemical impedance spectroscopy (EIS) frequency was kept between 200 kHz and 100 MHz with an alternating voltage amplitude of 10 mV. To avoid the
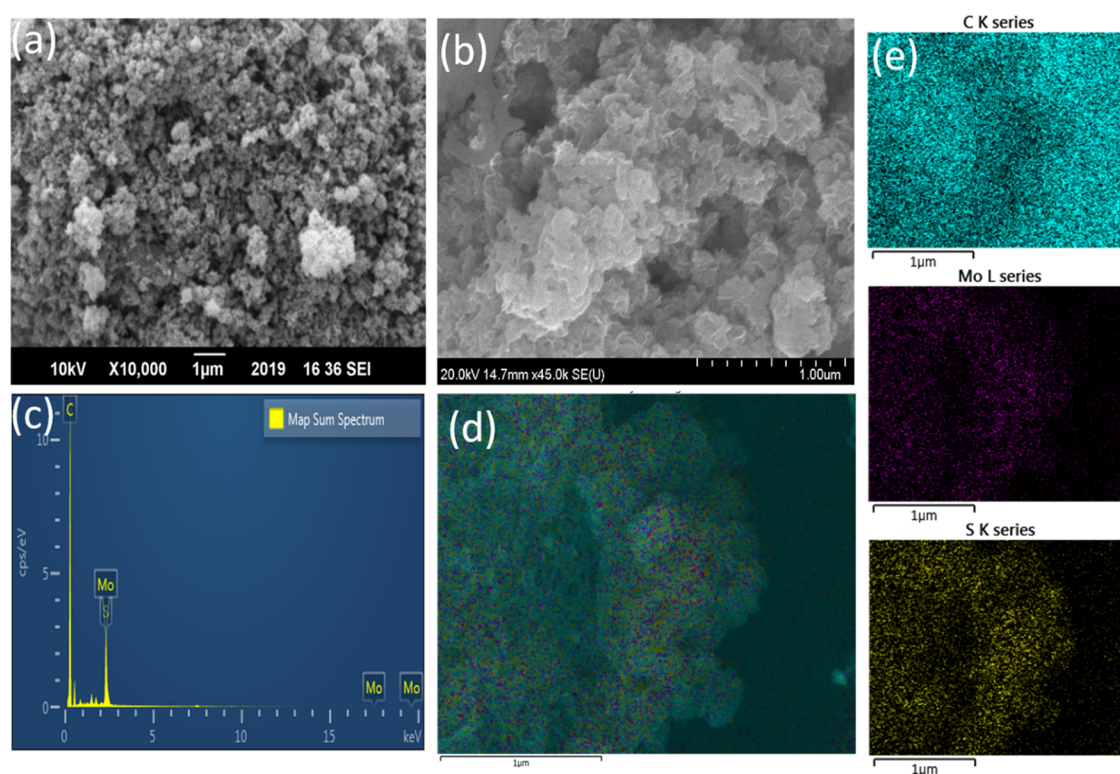
Figure 2. (a) SEM image of the spent methane reforming catalyst with graphitic carbon (GC), (b) FESEM of the spent catalyst after deposition of MoS_2, i.e., $MoS_2@GC$, (c) EDS elemental distribution graph for $MoS_2@GC$, and (d, e) EDS elemental mapping of $MoS_2@GC$.

misinterpretation of the rate-determining step, a large over-potential region was considered, and all of the abovementioned parameters were obtained from the quasi-steady-state polar-ization curves of the HER, which were *iR* correction from impedance data.

■ RESULTS AND DISCUSSION

Scanning electron microscopy provided an insight regarding the microstructure of GC and CNF grown over the spent catalyst. Figure 2a shows the SEM image of GC before fabrication, which shows deposition of adverse graphitic carbon on the surface of the catalyst, while abundant carbon nanofibers can be seen in Figure 3a. The field emission SEM (FESEM) images of $MoS_2@$ GC are given in Figure 2b, which clearly reveal the coverage of the spent catalyst with MoS_2. Energy-dispersive spectroscopy (EDS) point mapping (Figure 2c) of $MoS_2@GC$ shows the highest peak of 11 cps eV^{-1} for carbon with definite peaks of Mo and S, while the area mapping shows deposition of MoS_2 on graphitic carbon. Similarly, in Figure 3b carbon fibers with deposits can be seen, while innumerable thin nanoflakes with sizes of <100 nm are visible in the high-magnification FESEM image (Figure 3c). Furthermore, the EDS mapping of one of the larger aggregates under the corresponding FESEM conditions indicates the homogeneous distribution of carbon (C), molybdenum (Mo), and sulfur (S; Figure 3e,f). The atomic percentages of C, Mo, and S are 99.84, 0.11, and 0.05%, respectively, which altogether sum up to give a total of 100. From the atomic percent, the ratio of Mo and S that is 1:2 confirms the formation of pure MoS_2, ruling out the presence of any other compound of molybdenum and sulfur. Another important aspect that can be highlighted from the weight percentages of Mo, S, and C in $MoS_2@GC$ $MoS_2@CNF$ is the possibility of revitalization and enhancement in the performance

of spent catalysts with minimal usage of the material to be deposited.

Successful deposition of MoS_2 on the spent catalyst was performed using the environmentally friendly hydrothermal process, which can be confirmed through XRD. The crystalline phase of the spent catalyst and MoS_2 deposited on the spent catalyst was determined using XRD, the spectrum of which is shown in Figure 4a. The peaks of the spent catalyst at 19, 29, 33, 43, and 55° (JCPDFN 78-552) could be indexed to double-layered hydrotalcites with spinel-like structures, while the peaks at 12.1, 23, and 34° are associated with planer structures.[43,45] The peak common in all samples at $2\theta = 44$ and 51.7° corresponds to Ni(111) and Ni(200), respectively, embedded in the spent catalyst as well as present at the tip of fibers.[45] A distinguishable peak splitting in the diffraction pattern of all samples at ~26.1° is attributed to the (002) plane of carbon fiber and graphite formation after the calcination of hydrotalcite, which caused degeneration of the catalyst.[42,46] In the patterns of $MoS_2@GC$ and $MoS_2@CNF$, some prominent new peaks at 7.9, 32.7, and 58° appeared, which indicates the formation of the (001), (100), and (110) planes of single-phase MoS_2, according to the standard powdered diffraction file JCPDS 37-1492.[47] The appearance of these peaks with the absence of the (002) plane at $2\theta = 14°$ confirmed that partially exfoliated unstacked MoS_2 was formed, which is different from conventional 2H-MoS_2. This exfoliated MoS_2 was desired so that better electrochemical activity and conductivity could be achieved.[48,49] Most peaks that appeared in GC and CNF also appeared in $MoS_2@GC$ and $MoS_2@CNF$ but a visible decrease in peak intensity and peak positioning was observed. This suppression in the intensity of peaks can be attributed to the exfoliation of graphene and carbon nanofibers during synthesis and successful deposition of MoS_2
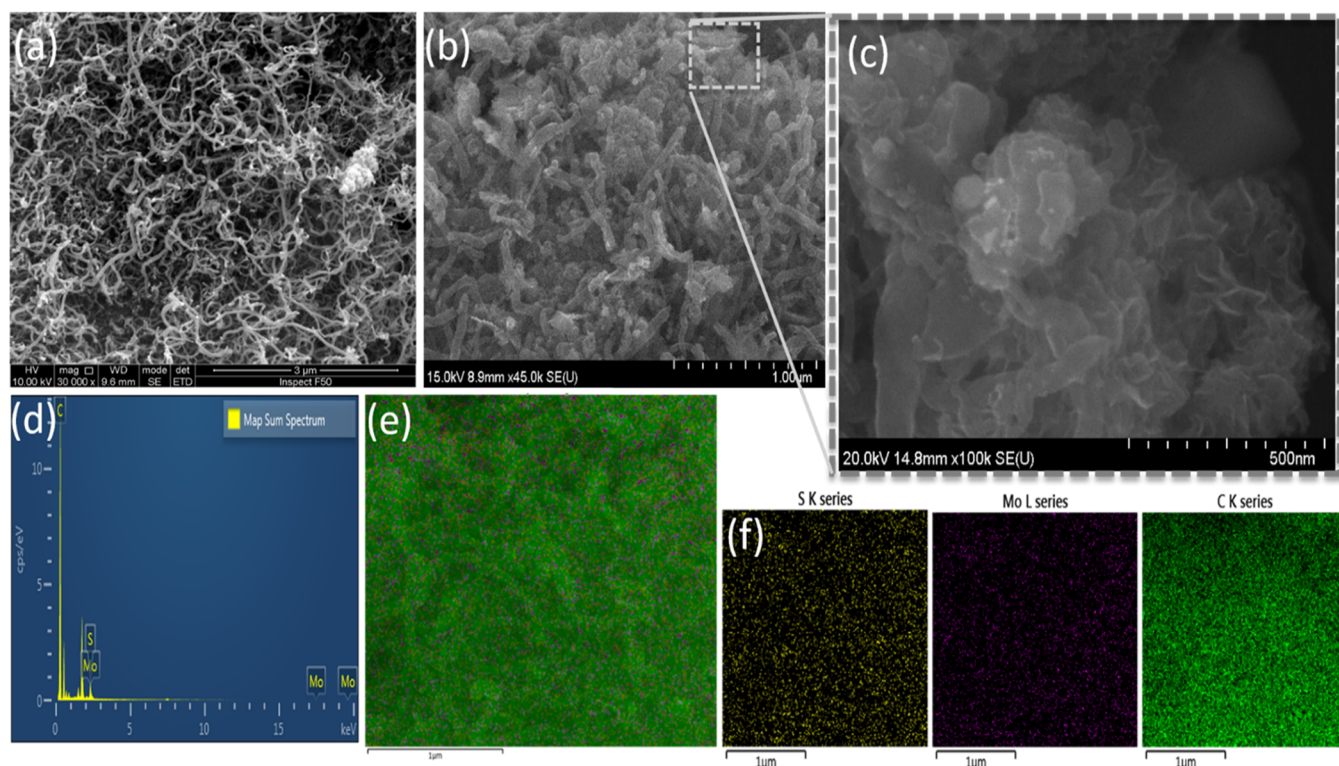
Figure 3. (a) FESEM images of the spent methane reforming catalyst with carbon nanofibers (CNF), (b) FESEM image of MoS_2 nanoflakes deposited on CNF, (d) EDS elemental distribution graph for MoS_2@CNF, and (e, f) EDS elemental mapping of MoS_2@CNF.
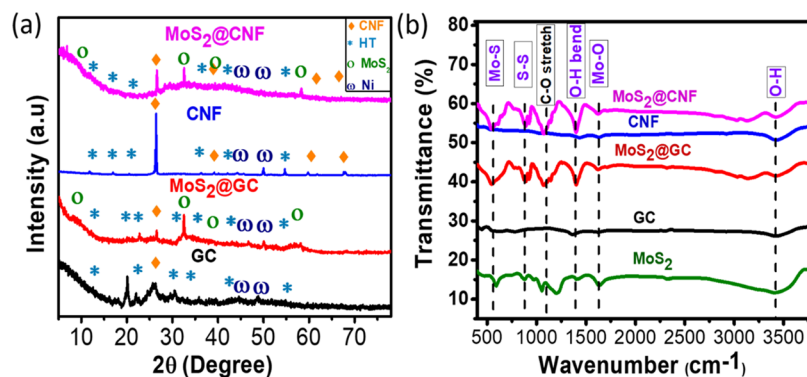

Figure 4. (a) XRD spectrum of GC, CNF, MoS_2@GC, and MoS_2@CNF. (b) FT-IR spectrum of the spent methane reforming catalyst with MoS_2, GC, CNF, MoS_2@GC, and MoS_2@CNF.

over the spent catalyst, which are accredited and supported by electron microscopy images.[50,51]

Chemical structures of MoS_2, spent GC and CNF, and newly formed MoS_2@CNF and MoS_2@GC were studied by FT-IR for acquiring the stretching and bending vibrations of functional groups in the samples, as shown in Figure 4b. In the spectrum of MoS_2, MoS_2@CNF, and MoS_2@GC, the perceptible peaks at 589, 880−960 cm^{-1}, and 1633−1637 cm^{-1} delineate the Mo−S, S−S, and Mo−O stretching vibrations, respectively, depicting the formation of MoS_2.[35,52] In the spectrum of CNF and GC, the peak at 1198 cm^{-1} can be attributed to the stretching vibrations of the carboxylic group, which indicates the growth of carbon fibers and graphitic carbon on the spent catalyst, while the peak at 1400 cm^{-1} depicts the disarranged structure of the interlayered spent catalyst with O−H bend, which was further disordered by hydrothermal treatment, providing more surface area where MoS_2 can get deposited.[53,54] The adsorption band at

3445 cm^{-1} is associated with the stretching vibration of the hydroxyl (−OH) functional group, and the intensity of O−H stretching is reduced in the nanostructured electrocatalyst because more MoS_2 was formed. The hydrazine hydrate used in the synthesis process acted as a reducing agent, which removed the water molecules from the synthesized electrocatalyst, resulting in lowering of O−H transmittance. The increase in the absorbance intensity of peaks in MoS_2@CNF and MoS_2@GC also clearly indicates the deposition of MoS_2 on the surface of the spent catalyst, which is supported by a laudable increase in the electrochemical activity of both newly fabricated catalysts. The performance of spent and newly fabricated electrocatalysts can be ascertained by performing electrochemical characterization.

Electrochemical Characterization. *Hydrogen Evolution Reaction.* The HER performance of all of the samples was evaluated in 1 M potassium hydroxide, which was used as an
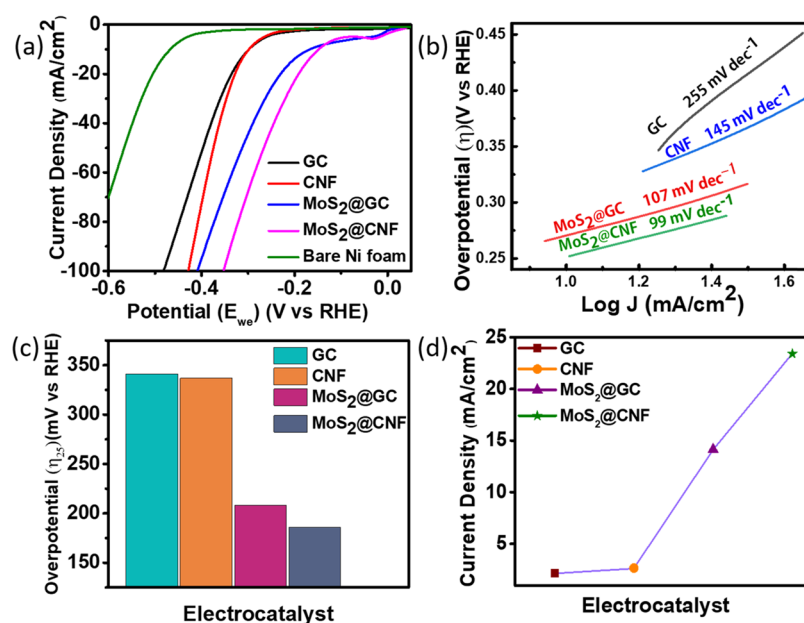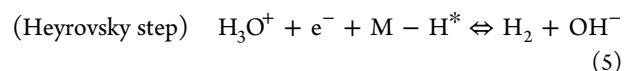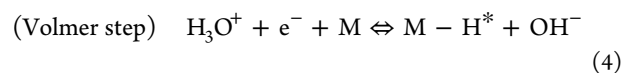
Figure 5. Electrochemical HER measurements of different catalysts. (a) Linear sweep voltammetry (LSV) polarization curve for bare Ni foam, GC, CNF, MoS_2@GC, and MoS_2@CNF; (b) corresponding Tafel slopes of spent GC and CNF, MoS_2@GC, and MoS_2@CNF; (c) overpotential comparison required at 25 mA cm^{-2}; and (d) current density of spent GC and CNF, and synthesized catalysts, i.e., MoS_2@CNF and MoS_2@GC at 200 mV versus RHE for the OER.

electrolyte, and the scan rate for LSV was kept at 10 mV s^{-1} for all samples. The HER performance of a catalyst in an alkaline medium is influenced by four major factors, i.e., adsorption of water on active sites, ability of the catalyst to dissociate adsorbed water, binding energy of hydrogen produced, and adsorption strength of aqueous OH$^-$. To know about the performance of an electrocatalyst, these factors are measured in terms of different parameters used in the modified Butler−Volmer equation, i.e., $\eta = \pm A \log_{10}(j/j\circ)$, which when generalized gives Tafel equation (i.e., $\eta = \alpha + b \log j$; where α and b are the transfer coefficient and Tafel slope, respectively).[55] The parameters used in the above equation are defined and analyzed as follows: (1) overpotential [(η) (V)]: the difference between the electrode potential (E) and the standard potential ($E°$); it is required for sustaining a current density of 10 mA cm^{-2} (η_{10}), (2) Tafel slope (V dec^{-1}; Figure 5b): the slope of the linear approximation of η versus log of current density, (3) exchange current density [($i°$) (mA cm^{-2})]: even in the absence of current, a dynamic equilibrium exists at the electrode/electrolyte interface, which results in the exchange of current density, and (4) mass-weighted HER current density (($i°_{0.2}$) (Ag^{-1}) at $\eta = 0.2$ V5).

As there is always some degree of uncertainty in the linearization of the Tafel slope and finding $i°$, additional current density at 0.2 V is introduced, which clarifies all ambiguities about the exact performance of the catalyst. For good activity, it is obvious for electrocatalysts to have lower η_{10}, higher $i°$, and higher. $i°_{0.2}$.[56] All of the parameters that determine the activity and performance of the catalysts are mentioned in Table S1 of which the best performance for the HER was shown by the newly formed electrocatalyst of MoS_2 and the spent catalyst. The synthesized nanostructured electrocatalyst exhibited an ample increase in activity with $\eta_{10} = 144$ mV, $i°_{0.2} = 10.63$ mA cm^{-2}, and $i° = 2.35$ mA cm^{-2} for MoS_2@CNF and $\eta_{10} = 0.165$ V, $i°_{0.2} = 6.733$ mA cm^{-2}, and $i° = 1.91$ mA cm^{-2} for MoS_2@GC, respectively. One of the crucial parameters mentioned above that aids in elucidating the HER mechanism is the Tafel slope. In

the Tafel slopes, a distinct difference before and after deposition of MoS_2 was observed. From GC (255 mV dec^{-1}) to MoS_2@GC (107 mV dec^{-1}) and from CNF (145 mV dec^{-1}) to MoS_2@CNF (99 mV dec^{-1}), major shifts of about 148 and 46 mV dec^{-1} were observed, respectively. From the range of the Tafel slopes, the mechanism with which the HER proceeds can be explained. Generally, the HER is described either by hydronium ion reduction or water reduction

(Volmer step) $H_3O^+ + e^- + M \Leftrightarrow M - H^* + OH^-$ (4)

(Heyrovsky step) $H_3O^+ + e^- + M - H^* \Leftrightarrow H_2 + OH^-$ (5)

(Tafel step) $2M - H^* \Leftrightarrow H_2 + 2M$ (6)

where the asterisk indicates the active site for the HER, and H* is a hydrogen atom bound to an active site. The HER in alkaline aqueous media proceeds in two steps (i.e., eqs 4−6). The discharge step (Volmer reaction) is the first step and either the reaction of atoms/ions (Heyrovsky reaction) or the combination of atoms (Tafel reaction) is the second step.[57] Typically, the Tafel slopes, as reckoned by the classic theory, for Tafel, Heyrovsky, and Volmer reactions are around 30, 40, and ≤ 120 mV dec^{-1}, respectively.[58] Although the Tafel slope is not an exclusive parameter for determining a specific followed mechanism but the obvious reduction in the slopes of MoS_2@CNF and MoS_2@GC confirms the Volmer−Heyrovsky pathway in HER kinetics.[59] The HER mechanism proceeds through the combination of metal hydrides instead of protonation of sulfur and this is because the adsorption energy of hydrogen to the surface of Mo (i.e., −3.29 eV) is greater than that of hydrogen to the surface of S (i.e, −2.78 eV). Moreover, the reaction kinetics can be improved through the synergistic effect of sulfur adjacent to the edge sites of Mo.[33]

The physical arguments supporting the lowest Tafel slopes, highest current densities, and highest exchange current densities
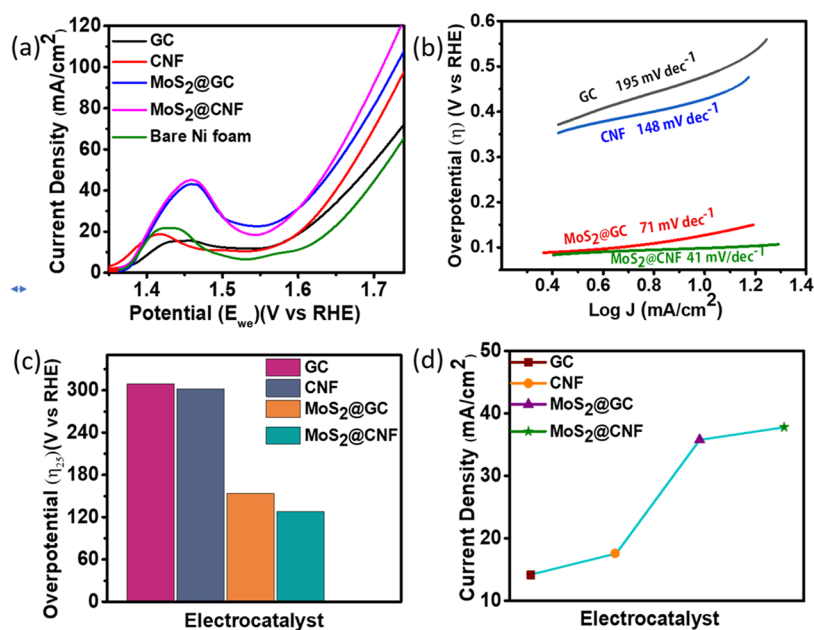
Figure 6. Electrochemical OER measurements of different catalysts. (a) Linear sweep voltammetry polarization curve; (b) corresponding Tafel slopes of spent GC and CNF, MoS_2@CNF, and MoS_2@GC; (c) overpotential required at 25 mA cm^{-2}; and (d) current density of spent GC and CNF, and synthesized catalysts, i.e., MoS_2@CNF and MoS_2@GC at 200 mV versus RHE for the OER.

of MoS_2@CNF are that the fibers and carbon deposits in the synthesized samples provided abundant surface area, shortened the diffusion distance, and provided a communicating platform for the conduction of electrons, while the deposition of MoS_2 enhanced not only the charge-transfer migration but also the dissociation of water and electrostatic affinity of OH$^-$, which improved the Volmer step and prevented the blockage of active sites by OH$^-$, making available more empty active sites and hence suggesting very low activation energy for the HER.[60] Due to the low requirement of activation energy, a lower overpotential is required to generate a certain current density.[61] Congruently, the obtained value of η_{10} is also low, indicating that the adsorption of water on active sites is less challenging, and the higher $i°$ of MoS_2@CNF and MoS_2@GC means that there is less hurdle for the flow of charges (electrons); therefore, the kinetics of the HER is intrinsically fast.[59] So, it can be asserted that MoS_2 and the carbon support collectively supplemented each other in enhancing the HER activity of MoS_2@CNF and MoS_2@GC.

The above results show that even by adding a small amount of MoS_2 to the spent catalyst, an ample increase of about 6-fold in the case of GC and about 5-fold in the case of CNF was obtained. Hence, from the obtained enhanced performance when compared with the reported MoS_2-based HER catalyst (Table S3), it can be said that not only our electrocatalysts show comparable activity but it can also be foreseen that utilization of spent catalysts and synthesized electrocatalysts with other dichalcogenides has greater capacity for further improvements to achieve a cleaner and carbon-free world of electrocatalysts.

Oxygen Evolution Reaction. The electrocatalytic performance of the spent catalyst and synthesized electrocatalysts was evaluated for the OER in a 1.0 M KOH aqueous solution using a three-electrode setup. The electrocatalytic activity of the spent catalysts, i.e., GC and CNF, and of newly fabricated MoS_2@GC and MoS_2@CNF was evaluated through the polarization curve of linear sweep voltammetry. The activity of MoS_2@GC and MoS_2@CNF was evaluated under similar conditions for the OER and HER. Figure 6a exhibits the polarization curves of the

spent catalyst and the synthesized electrocatalysts. In the OER polarization curves of all samples, a peak at a potential of about 1.36 V was first observed, which corresponds to the oxidation of Ni foam. In the curve of MoS_2@GC, a gradual increase in the current density was observed after 1.55 V, while in the curve of MoS_2@CNF, after 1.54 V, a sudden increase in the current density was observed. At a current density of 25 mA cm^{-2}, the spent catalysts, i.e., GC and CNF, showed overpotentials of about 309 and 302 mV while the fabricated catalysts, i.e., MoS_2@GC and MoS_2@CNF, displayed overpotentials of about 154 and 128 mV, respectively. At 200 mV, current densities of 14.9 mA cm^{-2} for GC and 17.6 mA cm^{-2} for CNF that after depositing with MoS_2 reached 35.7 and 37.8 mA cm^{-2} (Table S2) for MoS_2@GC and MoS_2@CNF, respectively.

The kinetics of the OER was gauged by Tafel plots i.e., Figure 6b. The lowest Tafel slopes of MoS_2@CNF (i.e., 41 mV dec^{-1}) and MoS_2@GC (i.e., 71 mV dec^{-1}) as compared to CNF (i.e., 148 mV dec^{-1}) and GC (i.e.,195 mV dec^{-1}) advocate for the faster kinetics of the fabricated catalysts. The graphitic carbon present on the spent catalyst decreases the interlayer stacking of MoS_2, resulting in exposed edge sites; furthermore, the transport of charges via the basal plane of MoS_2 is also favored,[62] while in the case of MoS_2@CNF, the electrocatalytic activity is improved due to the additional surface area of the fibers, providing more vacancy for water to adsorb, dissociate, and release oxygen and showing less affinity toward OH$^-$.[58] The highest exchange current densities revealed by MoS_2@CNF (i.e., $i° = 2.11$ mA cm^{-2}) and MoS_2@GC (i.e., $i° = 1.92$ mA cm^{-2}) when compared to those of CNF ($i° = 1.35$ mA cm^{-2}) and GC ($i° = 0.385$ mA cm^{-2}) show that the interfacial barrier for charge transfer is decreased due to which the kinetics of the OER is significantly improved. The oxygen evolution reaction (OER) is known as a two- or four-electron step and the reaction mechanism is complicated. Assuming a single-site mechanism, the following mechanism under alkaline conditions is considered
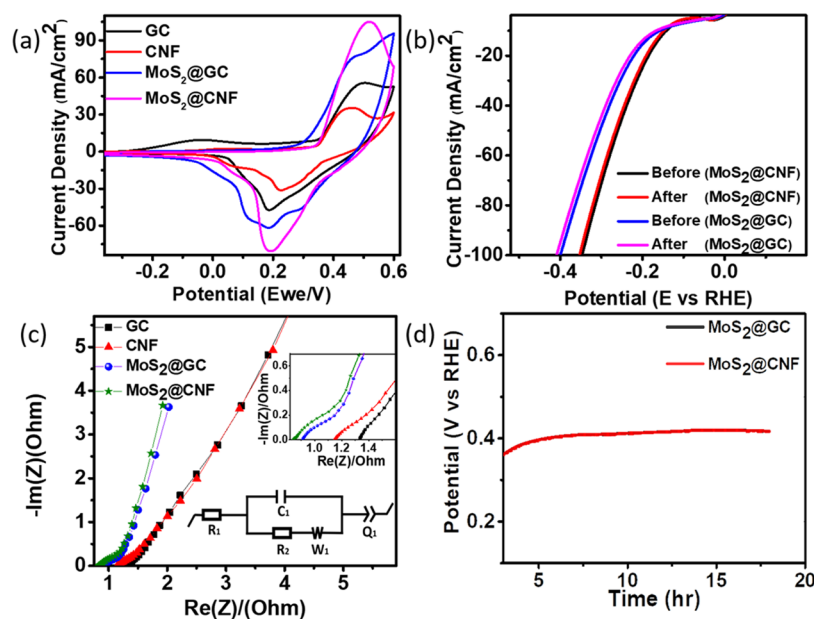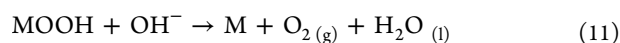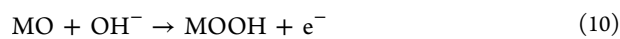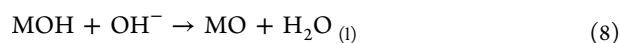
$$M + OH^- \rightarrow MOH^- \tag{7}$$

Figure 7. (a) Cyclic voltammetry (CV) curve of spent GC, CNF, and synthesized catalysts, i.e., MoS_2@GC and MoS_2@CNF. (b) Chronopotentiometry (CP) curve for MoS_2@CNF and MoS_2@GC for 18 h. (c) Nyquist plot for GC, CNF, MoS_2@CNF, and MoS_2@GC with the equivalent circuit diagram. (d) Linear sweep voltammetry results after the stability test.

$$MOH + OH^- \rightarrow MO + H_2O_{(l)} \qquad (8)$$

$$2MO \rightarrow 2M + O_{2\,(g)} \qquad (9)$$

$$MO + OH^- \rightarrow MOOH + e^- \qquad (10)$$

$$MOOH + OH^- \rightarrow M + O_{2\,(g)} + H_2O_{(l)} \qquad (11)$$

where M denotes a site on the surface or the surface of the electrocatalysts. As the Tafel slope is below 120 mV dec^{-1} and significantly low for the synthesized electrocatalysts; therefore, it can be asserted that the surface-adsorbed species produced in the early stage of the OER remains predominant.[63] Furthermore, it can be stated that in the alkaline medium during the electrocatalytic process, the produced OH^- likely get attached to the active sites (S) of MoS_2@CNF and MoS_2@GC and then reacted with other dissociating OH^- to form reaction intermediates (MOH, MO, and MOOH), which then on oxidation result in evolution of oxygen. The Tafel slope observed for MoS_2@CNF close to the characteristic value (40 mV dec^{-1}) of a mechanism involves pre-equilibrium consisting of a one-electron electrochemical step with a possible chemical step, followed by a one-electron electrochemical rate-determining step.[64] The activity of MoS_2@CNF is the best that is reported till far because the spent catalyst also possessed nickel atoms present at the tips of the fibers, which contributed to the transportation of charges, and the presence of active edge sites of intercalated MoS_2 is another reason for delivering better electrochemical performance.[34]

The electrostatic impedance measurements were biased to 0 V (vs the open-circuit voltage) using the three-electrode system, at a frequency ranging from 200 kHz to 100 MHz. The electrostatic impedance spectroscopy (EIS) of all of the samples possesses a semicircle and then an inclined line, which can be elaborated from the EIS spectrum shown in Figure 7c and the equivalent circuit (EC). Commonly, a simplified EC consisting of a capacitor and a resistor connected in parallel is an obvious model for carbon-based materials, but for complex nanostructures, the EC also changes.[65,66] In the impedance analysis for

MoS_2@CNF and MoS_2@GC, complications occur in the system and a simple RC circuit is not enough to be taken as the EC; therefore, with other circuit elements like R_1, R_2, C_1, and W_1, a constant phase element Q_1 (as shown in the inset of Figure 7c) was also introduced,[67] where R_1 is the ohmic resistance caused by solution (electrolyte), R_2 is the polarization resistance, C is the faradic capacitance, Z_w ascribes to the Warburg impedance,[68] and Q is a circuit component usually used to express an imperfect capacitor in a circuit of distributed resistors and capacitors.[69−71]

From the Bode plots for MoS_2@CNF and MoS_2@GC in Figures S6 and S7, respectively, it can be seen that the phase angle increases with increasing frequency, which is the typical behavior of the RC parallel circuit; therefore, C, R_2, and Z_w were modeled in parallel. In the spectrum of MoS_2@CNF and MoS_2@GC, it is noted that the spike-like region is more close to the imaginary axis, demonstrating fast charge-transfer kinetics and electric responses and mimicking a circuit with low resistance and large capacitance connected in parallel.[72] Contrary to that, in the impedance spectrum of the spent catalyst, there is a visible indication of the mass diffusion obstacles for ion or charge transfer in the electrode.[73] Moreover, from Table 1 and corresponding Figure 7c, it is also evident that the serial resistance (R_2) (intercept on real axis) and charge-transfer resistance (diameter of the semicircle) of MoS_2@CNF and MoS_2@GC are lower than those of the spent catalyst. The serial resistance is attributed to the intergranular electronic resistance between the active particles of the material and the

Table 1. Electrostatic Impedance Spectroscopy Data of All Samples

catalyst	R_1 (Ω)	C_1 (F)	R_2 (Ω)	Q_1 [F·s$(a-1)$]
GC	0.881	0.640	63.11	0.421
CNF	1.341	0.492	50.15	0.198
MoS_2@GC	0.946	0.621	0.627	0.928
MoS_2@CNF	0.838	0.570	8×10^{-4}	0.931

contact resistance between the active particles and the current collector, while the charge-transfer resistance (Z_w) originates at the interface of electrode/electrolyte caused by the diffusion process of ions or charge carriers, where the main charge carrier is the hydronium ion (H_3O^+).[74−76] With the good activity and conductivity of electrocatalysts, it is also required for electrocatalysts to be stable for which purpose stability tests like CV and chronopotentiometry (CP) are performed.

The comparative cyclic voltammograms of CNF, GC, MoS$_2$@CNF, and MoS$_2$@GC are shown in Figure 7a. In the potential range of −0.4 to −0.6 V at different scan rates ranging from 10 to 50 mV s^{-1}, these voltammograms were applied for assessing the performance of the spent and fabricated catalysts. In the profiles of MoS$_2$@CNF and MoS$_2$@GC, a pair of prominent, enhanced, and widely separated redox peaks, i.e., anodic (0.493 V) and cathodic (0.2 V) peaks, that are associated with the reduction and oxidation of metal centers involved in charge storage are observed, which is corroborating evidence for the typical form of a redox system corresponding to the generation of in situ efficient active sites for the OER and HER.[77,78]

When the CVs of GC and CNF and MoS$_2$@CNF are closely analyzed, the redox system bears the qualities of a typical form of electroactive charge storage devices (batteries), in which the mechanism involves reversible faradic reactions with charge transfer, and also those of pseudocapacitors, in which the mechanism involves the adsorption of electroactive ions onto the surface or near-surface region of electrode materials.[79,80] This kind of duality is a specialty of carbon fibers,[81] graphene,[82,83] or any carbon-based material[84,85] that are already in use as supercapacitors as well as pseudocapacitors where TMDs (specially MoS$_2$[86] and S$_2$V[87]) and oxides (like RuO$_2$[88,89] and MnO$_2$[90,91]) are also declared as good charge storage materials.[92,93] Congruently, the improvement in the performance of the spent catalyst after the addition of MoS$_2$ is due to the synergistic interfacial interaction between MoS$_2$ and carbon, which dispenses the effective migration of charge carriers from the layered edges of MoS$_2$ to the carbon support, hence contributing to an increase in current density of about 3−4 times by MoS$_2$@CNF, while of about 2-fold by MoS$_2$@GC for the HER and OER.[94,95]

Therefore, MoS$_2$@CNF and MoS$_2$@GC exhibit the widest CV curve with the highest redox peaks, thus showing the strongest electrochemical behavior as compared to CNF and GC. Moreover, increasing scan rates accordingly increase the current response, and the peak position slightly changes but the shape of CV curves retains, which indicates the good electrochemical stability and rate performance of MoS$_2$@CNF and MoS$_2$@GC, as displayed in Figures S4 and S5, respectively.

A long-term stability test is crucial for determining the effectiveness of electrocatalysts in the long run and for commercializing them for the production of oxygen and hydrogen fuels using renewable energy. The stability of MoS$_2$@CNF and MoS$_2$@GC was measured by exposing these electrocatalysts to CP in the same alkaline solution at 100 μA for 18 h. A stable behavior, as shown Figure 7d, is displayed by MoS$_2$@CNF and MoS$_2$@GC, which is primarily due to their stable structural characteristics. Due to the large interfacial interaction between the electrolyte and the electrode, there is low ion diffusion resistance that helps in quick ion penetration across the widely exposed active sites. Initially, the response of potential is rapid, but no prominent changes can be seen after the third hour. The probable reason for the change is the activation of the synthesized material during CP, the effect of

which can be visible in the form of a rapid potential response.[96] The LSV polarization curve in Figure 7b for the HER was obtained after testing the material for 1000 cycles of CV and performing CV at different scan rates, as shown in Figures S2 and S3 for MoS$_2$@CNF and MoS$_2$@GC, respectively, which clearly is a testimonial for the stability and activity of newly synthesized nanostructured electrocatalysts.

As a good OER catalyst may not be a good HER catalyst due to different rate-determining steps for respective reactions, which also limits the Butler−Volmer equation to describing chemically reversible electrocatalytic reactions,[63] but our catalysts have performed for both the HER and the OER.

■ CONCLUSIONS

Electrochemical water splitting is contemplated to be an effective solution to overcome energy crises and adverse environmental challenges. Many approaches have been carried out to build an economical and potent electrocatalyst. So, electrocatalysts consisting of spent methane reforming catalysts by in situ deposition of MoS$_2$ through a minimalistic and cost-effective hydrothermal method were synthesized. The successful formation of MoS$_2$@CNF and MoS$_2$@GC was confirmed by morphological and analytical characterization techniques; after assurance, these fabricated catalysts were tested for electrochemical HER and OER performances. The evaluation of the electrochemical performance of the fabricated catalysts showed lowest Tafel slopes, highest $i^{\circ}_{0.2}$, and low η_{25} for the OER and HER, indicating that the adsorption of OER and HER intermediates in MoS$_2$@CNF and MoS$_2$@GC catalysts was synergistically enhanced due to coupling of MoS$_2$ and the spent catalyst; meanwhile, the carbon present on the spent catalyst not only provided mechanical support for MoS$_2$ but also facilitated the electron transfer between MoS$_2$ and the alkaline solution. This work provided a promising demonstration of utilizing spent deactivated catalysts for electrochemical applications; moreover, it also gives a clear way forward for using carbon-deactivated catalysts with the addition of a very minimal amount of low-cost HER/OER catalysts for achieving accelerated overall water splitting.

■ ASSOCIATED CONTENT

Ⓢ Supporting Information

The Supporting Information is available free of charge at https://pubs.acs.org/doi/10.1021/acsomega.1c01558.

Electrochemical cell setup; electrochemical activity comparison of the spent reforming catalyst and the synthesized electrocatalysts; tabulated data of different parameters for the HER and OER; and comparison of MoS$_2$ with different carbon-based catalysts (PDF)

■ AUTHOR INFORMATION

Corresponding Author

Muhammad Taqi Mehran − *School of Chemical and Materials Engineering (SCME), National University of Sciences & Technology (NUST), Islamabad 44000, Pakistan;* ⊙ orcid.org/0000-0002-6045-6558; Phone: +92-51-9085-5115; Email: taqimehran@scme.nust.edu.pk

Authors

Muhammad Awais Khan − *School of Chemical and Materials Engineering (SCME), National University of Sciences & Technology (NUST), Islamabad 44000, Pakistan*

Salman Raza Naqvi − *School of Chemical and Materials Engineering (SCME), National University of Sciences & Technology (NUST), Islamabad 44000, Pakistan*

Asif Hussain Khoja − *Fossil Fuel Laboratory, Department of Thermal Energy Engineering, U.S.-Pakistan Centre for Advanced Studies in Energy (USPCASE), National University of Sciences & Technology (NUST), Islamabad 44000, Pakistan;* orcid.org/0000-0002-9006-3456

Faisal Shahzad − *Department of Metallurgy and Materials Engineering, Pakistan Institute of Engineering and Applied Sciences (PIEAS), Islamabad 45650, Pakistan;* orcid.org/0000-0002-1149-9674

Umair Sikander − *School of Chemical and Materials Engineering (SCME), National University of Sciences & Technology (NUST), Islamabad 44000, Pakistan*

Sajjad Hussain − *Department of Nanotechnology and Advanced Materials Engineering, Sejong University, Seoul 05006, Republic of Korea*

Ramsha Khan − *School of Chemical and Materials Engineering (SCME), National University of Sciences & Technology (NUST), Islamabad 44000, Pakistan*

Bilal Sarfaraz − *School of Chemical and Materials Engineering (SCME), National University of Sciences & Technology (NUST), Islamabad 44000, Pakistan*

Mutawara Mahmood Baig − *School of Chemical and Materials Engineering (SCME), National University of Sciences & Technology (NUST), Islamabad 44000, Pakistan*

Complete contact information is available at:
https://pubs.acs.org/10.1021/acsomega.1c01558

Notes
The authors declare no competing financial interest.

■ ACKNOWLEDGMENTS

■ REFERENCES

(1) Shukla, P. R.; Skea, J.; Calvo Buendia, E.; Masson-Delmotte, V.; Pörtner, H. O.; Roberts, D. C.; Zhai, P.; Slade, R.; Connors, S.; Van Diemen, R. et al. *Climate Change and Land: An IPCC Special Report on Climate Change, Desertification, Land Degradation, Sustainable Land Management, Food Security, and Greenhouse Gas Fluxes in Terrestrial Ecosystems*; Intergovernmental Panel on Climate Change (IPCC), 2019.

(2) Lubitz, W.; Tumas, W. Hydrogen: An Overview. *Chem. Rev.* **2007**, *107*, 3900−3903.

(3) Staffell, I.; Scamman, D.; Abad, A. V.; Balcombe, P.; Dodds, P. E.; Ekins, P.; Shah, N.; Ward, K. R. The Role of Hydrogen and Fuel Cells in the Global Energy System. *Energy Environ. Sci.* **2019**, *12*, 463−491.

(4) IEA. *Hydrogen*; International Energy Agency IEA, Paris, 2020; p 203.

(5) Yu, S.-B.; Lee, S.-H.; Mehran, M. T.; Hong, J.-E.; Lee, J.-W.; Lee, S.-B.; Park, S.-J.; Song, R.-H.; Shim, J.-H.; Shul, Y.-G.; Lim, T.-H. Syngas Production in High Performing Tubular Solid Oxide Cells by Using High-Temperature H2O/CO2 Co-Electrolysis. *Chem. Eng. J.* **2018**, *335*, 41−51.

(6) Mahmood, K.; Mehran, M. T.; Rehman, F.; Zafar, M. S.; Ahmad, S. W.; Song, R.-H. Electrosprayed Polymer-Hybridized Multidoped ZnO Mesoscopic Nanocrystals Yield Highly Efficient and Stable Perovskite Solar Cells. *ACS Omega* **2018**, *3*, 9648−9657.

(7) International Energy Agency *CO2 Capture and Storage: A Key Carbon Abatement Option*; OECDiLibrary, 2008.

(8) Bui, M.; Adjiman, C. S.; Bardow, A.; Anthony, E. J.; Boston, A.; Brown, S.; Fennell, P. S.; Fuss, S.; Galindo, A.; Hackett, L. A.; et al. Carbon Capture and Storage (CCS): The Way Forward. *Energy Environ. Sci.* **2018**, *11*, 1062−1176.

(9) Marafi, M.; Stanislaus, A. Spent Hydroprocessing Catalyst Management: A Review: Part II. Advances in Metal Recovery and Safe Disposal Methods. *Resour., Conserv. Recycl.* **2008**, *53*, 1−26.

(10) Chen, D.; Løding, R.; Anundskås, A.; Olsvik, O.; Holmen, A. Deactivation during Carbon Dioxide Reforming of Methane over Ni Catalyst: Microkinetic Analysis. *Chem. Eng. Sci.* **2001**, *56*, 1371−1379.

(11) Bradford, M. C. J.; Vannice, M. A. CO2 Reforming of CH4. *Catal. Rev.* **1999**, *41*, 1−42.

(12) Dufresne, P. Hydroprocessing Catalysts Regeneration and Recycling. *Appl. Catal., A* **2007**, *322*, 67−75.

(13) Ochoa, A.; Bilbao, J.; Gayubo, A. G.; Castaño, P. Coke Formation and Deactivation during Catalytic Reforming of Biomass and Waste Pyrolysis Products: A Review. *Renewable Sustainable Energy Rev.* **2020**, *119*, No. 109600.

(14) Han, J. W.; Park, J. S.; Choi, M. S.; Lee, H. Uncoupling the Size and Support Effects of Ni Catalysts for Dry Reforming of Methane. *Appl. Catal., B* **2017**, *203*, 625−632.

(15) Rashid, K.; Dong, S. K.; Mehran, M. T. Numerical Investigations to Determine the Optimal Operating Conditions for 1 KW-Class Flat-Tubular Solid Oxide Fuel Cell Stack. *Energy* **2017**, *141*, 673−691.

(16) Abbas, T.; Tahir, M.; Saidina Amin, N. A. Enhanced Metal–Support Interaction in Ni/Co3O4/TiO2 Nanorods toward Stable and Dynamic Hydrogen Production from Phenol Steam Reforming. *Ind. Eng. Chem. Res.* **2019**, *58*, 517−530.

(17) Peng, Q.; Tao, Y.; Ling, H.; Wu, Z.; Zhu, Z.; Jiang, R.; Zhao, Y.; Wang, Y.; Ji, C.; Liao, X.; et al. Tuning Hydrogen and Carbon Nanotube Production from Phenol Steam Reforming on Ni/Fe-Based Nanocatalysts. *ACS Sustainable Chem. Eng.* **2017**, *5*, 2098−2108.

(18) Zhang, C.; Yue, H.; Huang, Z.; Li, S.; Wu, G.; Ma, X.; Gong, J. Hydrogen Production via Steam Reforming of Ethanol on Phyllosilicate-Derived Ni/SiO2: Enhanced Metal–Support Interaction and Catalytic Stability. *ACS Sustainable Chem. Eng.* **2013**, *1*, 161−173.

(19) Tu, P. H.; Le, D. N.; Dao, T. D.; Tran, Q.-T.; Doan, T. C. D.; Shiratori, Y.; Dang, C. M. Structured Catalyst Containing CeO2–Ni Flowers for Dry Reforming of Methane. *Int. J. Hydrogen Energy* **2020**, *45*, 18363−18375.

(20) Kuvshinov, G. G.; Chukanov, I. S.; Krutsky, Y. L.; Ochkov, V. V.; Zaikovskii, V. I.; Kuvshinov, D. G. Changes in the Properties of Fibrous Nanocarbons during High Temperature Heat Treatment. *Carbon* **2009**, *47*, 215−225.

(21) Kim, J.; Im, U.-S.; Peck, D.-H.; Yoon, S.-H.; Park, H. S.; Jung, D.-H. Enhanced Activity and Durability of the Oxygen Reduction Catalysts Supported on the Surface Expanded Tubular-Type Carbon Nanofiber. *Appl. Catal., B* **2017**, *217*, 192−200.

(22) Chinthaginjala, J. K.; Seshan, K.; Lefferts, L. Preparation and Application of Carbon-Nanofiber Based Microstructured Materials as Catalyst Supports. *Ind. Eng. Chem. Res.* **2007**, *46*, 3968−3978.

(23) Lee, Y.; Suntivich, J.; May, K. J.; Perry, E. E.; Shao-Horn, Y. Synthesis and Activities of Rutile IrO2 and RuO2 Nanoparticles for Oxygen Evolution in Acid and Alkaline Solutions. *J. Phys. Chem. Lett.* **2012**, *3*, 399−404.

(24) Wang, P.; Zhang, X.; Zhang, J.; Wan, S.; Guo, S.; Lu, G.; Yao, J.; Huang, X. Precise Tuning in Platinum-Nickel/Nickel Sulfide Interface Nanowires for Synergistic Hydrogen Evolution Catalysis. *Nat. Commun.* **2017**, *8*, No. 14580.

(25) Park, S.; Shao, Y.; Liu, J.; Wang, Y. Oxygen Electrocatalysts for Water Electrolyzers and Reversible Fuel Cells: Status and Perspective. *Energy Environ. Sci.* **2012**, *5*, 9331−9344.

(26) McCrory, C. C. L.; Jung, S.; Ferrer, I. M.; Chatman, S. M.; Peters, J. C.; Jaramillo, T. F. Benchmarking Hydrogen Evolving Reaction and Oxygen Evolving Reaction Electrocatalysts for Solar Water Splitting Devices. *J. Am. Chem. Soc.* **2015**, *137*, 4347−4357.

(27) Tiwari, J. N.; Sultan, S.; Myung, C. W.; Yoon, T.; Li, N.; Ha, M.; Harzandi, A. M.; Park, H. J.; Kim, D. Y.; Chandrasekaran, S. S.; et al. Multicomponent Electrocatalyst with Ultralow Pt Loading and High Hydrogen Evolution Activity. *Nat. Energy* **2018**, *3*, 773−782.

(28) Lv, F.; Feng, J.; Wang, K.; Dou, Z.; Zhang, W.; Zhou, J.; Yang, C.; Luo, M.; Yang, Y.; Li, Y.; et al. Iridium–Tungsten Alloy Nanodendrites as PH-Universal Water-Splitting Electrocatalysts. *ACS Cent. Sci.* **2018**, *4*, 1244−1252.

(29) Xia, X.; Wang, L.; Sui, N.; Colvin, V. L.; William, W. Y. Recent Progress in Transition Metal Selenide Electrocatalysts for Water Splitting. *Nanoscale* **2020**, *12*, 12249−12262.

(30) Yin, J.; Jin, J.; Lin, H.; Yin, Z.; Li, J.; Lu, M.; Guo, L.; Xi, P.; Tang, Y.; Yan, C.-H. Optimized Metal Chalcogenides for Boosting Water Splitting. *Adv. Sci.* **2020**, *7*, No. 1903070.

(31) Liao, M.; Zhang, Q.; Schwarz, W. H. E. Properties and Stabilities of MX, MX2, and M2X2 Compounds (M = Zn, Cd, Hg; X = F, Cl, Br, I). *Inorg. Chem.* **1995**, *34*, 5597−5605.

(32) Rashid, K.; Dong, S. K.; Mehran, M. T.; Lee, D. W. Design and Analysis of Compact Hotbox for Solid Oxide Fuel Cell Based 1 KW-Class Power Generation System. *Appl. Energy* **2017**, *208*, 620−636.

(33) Li, L.; Qin, Z.; Ries, L.; Hong, S.; Michel, T.; Yang, J.; Salameh, C.; Bechelany, M.; Miele, P.; Kaplan, D.; et al. Role of Sulfur Vacancies and Undercoordinated Mo Regions in MoS2 Nanosheets toward the Evolution of Hydrogen. *ACS Nano* **2019**, *13*, 6824−6834.

(34) Wu, J.; Liu, M.; Chatterjee, K.; Hackenberg, K. P.; Shen, J.; Zou, X.; Yan, Y.; Gu, J.; Yang, Y.; Lou, J.; Ajayan, P. M. Exfoliated 2D Transition Metal Disulfides for Enhanced Electrocatalysis of Oxygen Evolution Reaction in Acidic Medium. *Adv. Mater. Interfaces* **2016**, *3*, No. 1500669.

(35) Khatri, R.; Puri, N. K. Electrochemical Study of Hydrothermally Synthesised Reduced MoS2 Layered Nanosheets. *Vacuum* **2020**, *175*, No. 109250.

(36) Acerce, M.; Voiry, D.; Chhowalla, M. Metallic 1T Phase MoS 2 Nanosheets as Supercapacitor Electrode Materials. *Nat. Nanotechnol.* **2015**, *10*, 313−318.

(37) Lin, Y.-C.; Dumcenco, D. O.; Huang, Y.-S.; Suenaga, K. Atomic Mechanism of the Semiconducting-to-Metallic Phase Transition in Single-Layered MoS 2. *Nat. Nanotechnol.* **2014**, *9*, 391−396.

(38) Ma, W.; Li, H.; Jiang, S.; Han, G.; Gao, J.; Yu, X.; Lian, H.; Tu, W.; Han, Y.; Ma, R. Facile Synthesis of Superstructured MoS2 and Graphitic Nanocarbon Hybrid for Efficient Hydrogen Evolution Reaction. *ACS Sustainable Chem. Eng.* **2018**, *6*, 14441−14449.

(39) Chen, Y. M.; Yu, X. Y.; Li, Z.; Paik, U.; Lou, X. W. D. Hierarchical MoS2 Tubular Structures Internally Wired by Carbon Nanotubes as a Highly Stable Anode Material for Lithium-Ion Batteries. *Sci. Adv.* **2016**, *2*, No. e1600021.

(40) Li, W.; Zhang, Z.; Zhang, W.; Zou, S. MoS2 Nanosheets Supported on Hollow Carbon Spheres as Efficient Catalysts for Electrochemical Hydrogen Evolution Reaction. *ACS Omega* **2017**, *2*, 5087−5094.

(41) Hou, X.; Zhou, H.; Zhao, M.; Cai, Y.; Wei, Q. MoS2 Nanoplates Embedded in Co–N-Doped Carbon Nanocages as Efficient Catalyst for HER and OER. *ACS Sustainable Chem. Eng.* **2020**, *8*, 5724−5733.

(42) Xiong, X.; Luo, W.; Hu, X.; Chen, C.; Qie, L.; Hou, D.; Huang, Y. Flexible Membranes of MoS 2/C Nanofibers by Electrospinning as Binder-Free Anodes for High-Performance Sodium-Ion Batteries. *Sci. Rep.* **2015**, *5*, No. 9254.

(43) Sikander, U.; Samsudin, M. F.; Sufian, S.; KuShaari, K.; Kait, C. F.; Naqvi, S. R.; Chen, W.-H. Tailored Hydrotalcite-Based Mg-Ni-Al Catalyst for Hydrogen Production via Methane Decomposition: Effect of Nickel Concentration and Spinel-like Structures. *Int. J. Hydrogen Energy* **2019**, *44*, 14424−14433.

(44) Li, M.; Wang, D.; Li, J.; Pan, Z.; Ma, H.; Jiang, Y.; Tian, Z. Facile Hydrothermal Synthesis of MoS 2 Nano-Sheets with Controllable Structures and Enhanced Catalytic Performance for Anthracene Hydrogenation. *RSC Adv.* **2016**, *6*, 71534−71542.

(45) Li, M.; Wang, X.; Li, S.; Wang, S.; Ma, X. Hydrogen Production from Ethanol Steam Reforming over Nickel Based Catalyst Derived from Ni/Mg/Al Hydrotalcite-like Compounds. *Int. J. Hydrogen Energy* **2010**, *35*, 6699−6708.

(46) Wang, F.; Wang, T.; Sun, S.; Xu, Y.; Yu, R.; Li, H. One-Step Synthesis of Nickle Iron-Layered Double Hydroxide/Reduced Graphene Oxide/Carbon Nanofibres Composite as Electrode Materials for Asymmetric Supercapacitor. *Sci. Rep.* **2018**, *8*, No. 8908.

(47) Zafiropoulou, I.; Katsiotis, M. S.; Boukos, N.; Karakassides, M. A.; Stephen, S.; Tzitzios, V.; Fardis, M.; Vladea, R. V.; Alhassan, S. M.; Papavassiliou, G. In Situ Deposition and Characterization of MoS2 Nanolayers on Carbon Nanofibers and Nanotubes. *J. Phys. Chem. C* **2013**, *117*, 10135−10142.

(48) Zhao, X.; Zhu, H.; Yang, X. Amorphous Carbon Supported MoS 2 Nanosheets as Effective Catalysts for Electrocatalytic Hydrogen Evolution. *Nanoscale* **2014**, *6*, 10680−10685.

(49) Li, Y.; Wang, L.; Zhang, S.; Dong, X.; Song, Y.; Cai, T.; Liu, Y. Cracked Monolayer 1T MoS 2 with Abundant Active Sites for Enhanced Electrocatalytic Hydrogen Evolution. *Catal. Sci. Technol.* **2017**, *7*, 718−724.

(50) Holder, C. F.; Schaak, R. E. Tutorial on Powder X-Ray Diffraction for Characterizing Nanoscale Materials. *ACS Nano* **2019**, *13*, 7359−7365.

(51) Wang, S.; Zhang, D.; Li, B.; Zhang, C.; Du, Z.; Yin, H.; Bi, X.; Yang, S. Ultrastable In-Plane 1T–2H MoS 2 Heterostructures for Enhanced Hydrogen Evolution Reaction. *Adv. Energy Mater.* **2018**, *8*, No. 1801345.

(52) Huang, K.-J.; Wang, L.; Liu, Y.-J.; Wang, H.-B.; Liu, Y.-M.; Wang, L.-L. Synthesis of Polyaniline/2-Dimensional Graphene Analog MoS2 Composites for High-Performance Supercapacitor. *Electrochim. Acta* **2013**, *109*, 587−594.

(53) Tong, Z.; Ma, Q.; Ni, Y.; Mei, T.; Li, J.; Dong, G. Tribological Properties of Carbon Fabric Reinforced Phenolic-Based Composites Containing CNTs@ MoS 2 Hybrids. *J. Mater. Sci.* **2019**, *54*, 14354−14366.

(54) Sikander, U.; Sufian, S.; Salam, M. A.; et al. Synthesis and Structural Analysis of Double Layered Ni-Mg-Al Hydrotalcite like Catalyst. *Procedia Eng.* **2016**, *148*, 261−267.

(55) Cha, S.-W.; O'Hayre, R.; Colella, W.; Prinz, F. Chapter 3: Fuel Cell Reaction Kinetics. In *Fuel Cell Fundamentals*; John Wiley & Sons, Ltd., 2016; pp 77−116.

(56) Chatti, M.; Gengenbach, T.; King, R.; Spiccia, L.; Simonov, A. N. Vertically Aligned Interlayer Expanded MoS2 Nanosheets on a Carbon Support for Hydrogen Evolution Electrocatalysis. *Chem. Mater.* **2017**, *29*, 3092−3099.

(57) Laursen, A. B.; Kegnæs, S.; Dahl, S.; Chorkendorff, I. Molybdenum Sulfides—Efficient and Viable Materials for Electro- and Photoelectrocatalytic Hydrogen Evolution. *Energy Environ. Sci.* **2012**, *5*, 5577−5591.

(58) Thomas, J. G. N. Kinetics of Electrolytic Hydrogen Evolution and the Adsorption of Hydrogen by Metals. *Trans. Faraday Soc.* **1961**, *57*, 1603−1611.

(59) Anjum, M. A. R.; Jeong, H. Y.; Lee, M. H.; Shin, H. S.; Lee, J. S. Efficient Hydrogen Evolution Reaction Catalysis in Alkaline Media by All-in-One MoS2 with Multifunctional Active Sites. *Adv. Mater.* **2018**, *30*, No. 1707105.

(60) Hu, C.; Zhang, L.; Gong, J. Recent Progress Made in the Mechanism Comprehension and Design of Electrocatalysts for Alkaline Water Splitting. *Energy Environ. Sci.* **2019**, *12*, 2620−2645.

(61) Yang, L.; Zhou, W.; Lu, J.; Hou, D.; Ke, Y.; Li, G.; Tang, Z.; Kang, X.; Chen, S. Hierarchical Spheres Constructed by Defect-Rich MoS2/Carbon Nanosheets for Efficient Electrocatalytic Hydrogen Evolution. *Nano Energy* **2016**, *22*, 490−498.

(62) Pandey, A.; Mukherjee, A.; Chakrabarty, S.; Chanda, D.; Basu, S. Interface Engineering of an RGO/MoS2/Pd 2D Heterostructure for Electrocatalytic Overall Water Splitting in Alkaline Medium. *ACS Appl. Mater. Interfaces* **2019**, *11*, 42094−42103.

(63) Shinagawa, T.; Garcia-Esparza, A. T.; Takanabe, K. Insight on Tafel Slopes from a Microkinetic Analysis of Aqueous Electrocatalysis for Energy Conversion. *Sci. Rep.* **2015**, *5*, No. 13801.

(64) Lu, Z.; Xu, W.; Zhu, W.; Yang, Q.; Lei, X.; Liu, J.; Li, Y.; Sun, X.; Duan, X. Three-Dimensional NiFe Layered Double Hydroxide Film for High-Efficiency Oxygen Evolution Reaction. *Chem. Commun.* **2014**, *50*, 6479−6482.

(65) Song, X.; Qi, Q.; Zhang, T.; Wang, C. A Humidity Sensor Based on KCl-Doped SnO2 Nanofibers. *Sens. Actuators, B* **2009**, *138*, 368−373.

(66) Su, M.; Wang, J. Preparation and Humidity Sensitivity of Multi-Layered Zirconia Thin Films by Sol–Gel Method. *Sens. Lett.* **2011**, *9*, 670−674.

(67) Han, K. I.; Kim, S.; Yang, W. S.; Kim, H. S.; Shin, M.; Kim, J. P.; Lee, I. G.; Cho, B. J.; Hwang, W. S. Material Characteristics and Equivalent Circuit Models of Stacked Graphene Oxide for Capacitive Humidity Sensors. *AIP Adv.* **2016**, *6*, No. 35203.

(68) Zhang, D.; Liu, J.; Xia, B. Layer-by-Layer Self-Assembly of Zinc Oxide/Graphene Oxide Hybrid toward Ultrasensitive Humidity Sensing. *IEEE Electron Device Lett.* **2016**, *37*, 916−919.

(69) Hirschorn, B.; Orazem, M. E.; Tribollet, B.; Vivier, V.; Frateur, I.; Musiani, M. Constant-Phase-Element Behavior Caused by Resistivity Distributions in Films: I. Theory. *J. Electrochem. Soc.* **2010**, *157*, No. C452.

(70) Zhang, D.; Zong, X.; Wu, Z.; Zhang, Y. Ultrahigh-Performance Impedance Humidity Sensor Based on Layer-by-Layer Self-Assembled Tin Disulfide/Titanium Dioxide Nanohybrid Film. *Sens. Actuators, B* **2018**, *266*, 52−62.

(71) Zhang, D.; Tong, J.; Xia, B.; Xue, Q. Ultrahigh Performance Humidity Sensor Based on Layer-by-Layer Self-Assembly of Graphene Oxide/Polyelectrolyte Nanocomposite Film. *Sens. Actuators, B* **2014**, *203*, 263−270.

(72) Lai, L.; Wang, L.; Yang, H.; Sahoo, N. G.; Tam, Q. X.; Liu, J.; Poh, C. K.; Lim, S. H.; Shen, Z.; Lin, J. Tuning Graphene Surface Chemistry to Prepare Graphene/Polypyrrole Supercapacitors with Improved Performance. *Nano Energy* **2012**, *1*, 723−731.

(73) Ke, Q.; Zheng, M.; Liu, H.; Guan, C.; Mao, L.; Wang, J. 3D TiO 2@ Ni (OH) 2 Core-Shell Arrays with Tunable Nanostructure for Hybrid Supercapacitor Application. *Sci. Rep.* **2015**, *5*, No. 13940.

(74) Jiang, K.; Fei, T.; Zhang, T. Humidity Sensor Using a Li-Loaded Microporous Organic Polymer Assembled by 1, 3, 5-Trihydroxyben-zene and Terephthalic Aldehyde. *RSC Adv.* **2014**, *4*, 28451−28455.

(75) Girija, T. C.; Sangaranarayanan, M. V. Analysis of Polyaniline-Based Nickel Electrodes for Electrochemical Supercapacitors. *J. Power Sources* **2006**, *156*, 705−711.

(76) Portet, C.; Taberna, P. L.; Simon, P.; Laberty-Robert, C. Modification of Al Current Collector Surface by Sol–Gel Deposit for Carbon–Carbon Supercapacitor Applications. *Electrochim. Acta* **2004**, *49*, 905−912.

(77) Zhang, Y.; He, T.; Liu, G.; Zu, L.; Yang, J. One-Pot Mass Preparation of MoS 2/C Aerogels for High-Performance Super-capacitors and Lithium-Ion Batteries. *Nanoscale* **2017**, *9*, 10059−10066.

(78) Yang, Y.; Zhang, K.; Lin, H.; Li, X.; Chan, H. C.; Yang, L.; Gao, Q. MoS2–Ni3S2 Heteronanorods as Efficient and Stable Bifunctional Electrocatalysts for Overall Water Splitting. *ACS Catal.* **2017**, *7*, 2357−2366.

(79) Liu, J.; Wang, J.; Xu, C.; Jiang, H.; Li, C.; Zhang, L.; Lin, J.; Shen, Z. X. Advanced Energy Storage Devices: Basic Principles, Analytical Methods, and Rational Materials Design. *Adv. Sci.* **2018**, *5*, No. 1700322.

(80) Gogotsi, Y.; Penner, R. M. Energy Storage in Nanomaterials–Capacitive, Pseudocapacitive, or Battery-Like? *ACS Nano.* **2018**, *12*, 2081−2083.

(81) Senokos, E.; Reguero, V.; Palma, J.; Vilatela, J. J.; Marcilla, R. Macroscopic Fibres of CNTs as Electrodes for Multifunctional Electric Double Layer Capacitors: From Quantum Capacitance to Device Performance. *Nanoscale* **2016**, *8*, 3620−3628.

(82) Yang, X.; Cheng, C.; Wang, Y.; Qiu, L.; Li, D. Liquid-Mediated Dense Integration of Graphene Materials for Compact Capacitive Energy Storage. *Science* **2013**, *341*, 534−537.

(83) Miller, J. R.; Outlaw, R. A.; Holloway, B. C. Graphene Double-Layer Capacitor with Ac Line-Filtering Performance. *Science* **2010**, *329*, 1637−1639.

(84) Fuertes, A. B.; Sevilla, M. Superior Capacitive Performance of Hydrochar-Based Porous Carbons in Aqueous Electrolytes. *ChemSusChem* **2015**, *8*, 1049−1057.

(85) Raymundo-Piñero, E.; Kierzek, K.; Machnikowski, J.; Béguin, F. Relationship between the Nanoporous Texture of Activated Carbons and Their Capacitance Properties in Different Electrolytes. *Carbon* **2006**, *44*, 2498−2507.

(86) Zhang, B.; Ji, X.; Xu, K.; Chen, C.; Xiong, X.; Xiong, J.; Yao, Y.; Miao, L.; Jiang, J. Unraveling the Different Charge Storage Mechanism in T and H Phases of MoS2. *Electrochim. Acta* **2016**, *217*, 1−8.

(87) Liang, X.; Chen, M.; Zhu, H.; Zhu, H.; Cui, X.; Yan, J.; Chen, Q.; Xia, X.; Liu, Q. Unveiling the Solid-Solution Charge Storage Mechanism in 1T Vanadium Disulfide Nanoarray Cathodes. *J. Mater. Chem. A* **2020**, *8*, 9068−9076.

(88) Xia, H.; Meng, Y. S.; Yuan, G.; Cui, C.; Lu, L. A Symmetric RuO2/RuO2 Supercapacitor Operating at 1.6 V by Using a Neutral Aqueous Electrolyte. *Electrochem. Solid State Lett.* **2012**, *15*, No. A60.

(89) Subramanian, V.; Hall, S. C.; Smith, P. H.; Rambabu, B. Mesoporous Anhydrous RuO2 as a Supercapacitor Electrode Material. *Solid State Ionics* **2004**, *175*, 511−515.

(90) Jiang, H.; Li, C.; Sun, T.; Ma, J. A Green and High Energy Density Asymmetric Supercapacitor Based on Ultrathin MnO 2 Nanostructures and Functional Mesoporous Carbon Nanotube Electrodes. *Nanoscale* **2012**, *4*, 807−812.

(91) Jiang, H.; Sun, T.; Li, C.; Ma, J. Hierarchical Porous Nanostructures Assembled from Ultrathin MnO 2 Nanoflakes with Enhanced Supercapacitive Performances. *J. Mater. Chem.* **2012**, *22*, 2751−2756.

(92) Cook, J. B.; Kim, H.-S.; Lin, T. C.; Lai, C.-H.; Dunn, B.; Tolbert, S. H. Pseudocapacitive Charge Storage in Thick Composite MoS2 Nanocrystal-Based Electrodes. *Adv. Energy Mater.* **2017**, *7*, No. 1601283.

(93) Cong, X.; Cheng, C.; Liao, Y.; Ye, Y.; Dong, C.; Sun, H.; Ji, X.; Zhang, W.; Fang, P.; Miao, L.; et al. Intrinsic Charge Storage Capability of Transition Metal Dichalcogenides as Pseudocapacitor Electrodes. *J. Phys. Chem. C* **2015**, *119*, 20864−20870.

(94) Zhao, H.; Zeng, H.; Wu, Y.; Zhang, S.; Li, B.; Huang, Y. Facile Scalable Synthesis and Superior Lithium Storage Performance of Ball-Milled MoS 2–Graphite Nanocomposites. *J. Mater. Chem. A* **2015**, *3*, 10466−10470.

(95) Kim, M.; Kim, Y. K.; Kim, J.; Cho, S.; Lee, G.; Jang, J. Fabrication of a Polyaniline/MoS 2 Nanocomposite Using Self-Stabilized Dispersion Polymerization for Supercapacitors with High Energy Density. *RSC Adv.* **2016**, *6*, 27460−27465.

(96) Khan, R.; Mehran, M. T.; Baig, M. M.; Sarfraz, B.; Naqvi, S. R.; Niazi, M. B. K.; Khan, M. Z.; Khoja, A. H. 3D Hierarchical Heterostructured LSTN@ NiMn-Layered Double Hydroxide as a Bifunctional Water Splitting Electrocatalyst for Hydrogen Production. *Fuel* **2020**, *285*, No. 119174.